©ESO 2026

Ultraluminous X-ray sources in the first eROSITA survey

I. Candidate catalogs

P. Weber[1], T. P. Roberts[2], S. Hämmerich[1], E. Kyritsis[4,3,6], A. Zezas[4,3], M. G. F. Mayer[1], A. Zainab[1], I. Kreykenbohm[1], A. Merloni[6], M. Sasaki[1], A. Schwope[5], M. Middleton[7], A. Basu-Zych[9,10], A. Hornschemeier[9,11], N. Vulic[8,9,10,12], M. Salvato[6], N. Webb[13], H. Tranin[14,15], N. Schettino[1], C. Kirsch[1], S. Saeedi[1], F. Zangrandi[1], M. Lorenz[1], L. Dauner[1], T. Dauser[1], F. Haberl[6], C. Maitra[17,6], Z. Igo[6], A. Santangelo[16], L. Ducci[16], and J. Wilms[1]

[1] Dr. Karl Remeis-Sternwarte and Erlangen Centre for Astroparticle Physics, Friedrich-Alexander Universität Erlangen-Nürnberg, Sternwartstr. 7, 96049 Bamberg, Germany
e-mail: philipp.ph.weber@fau.de
[2] Centre for Extragalactic Astronomy & Dept of Physics, Durham University, South Road, Durham DH1 3LE, UK
[3] Institute of Astrophysics, Foundation for Research and Technology-Hellas, GR 71110 Heraklion, Greece
[4] Physics Department, & Institute of Theoretical and Computational Physics, University of Crete, GR 71003, Heraklion, Greece
[5] Leibniz-Institut für Astrophysik Potsdam, An der Sternwarte 16, 14482 Potsdam, Germany
[6] Max-Planck-Institut für Extraterrestrische Physik, Gießenbachstraße 1, 85748 Garching, Germany
[7] School of Physics and Astronomy, University of Southampton, Highfield, Southampton SO17 1BJ, UK
[8] Eureka Scientific, Inc., 2452 Delmer St., Suite 100, Oakland, CA 94602-3017, USA
[9] NASA Goddard Space Flight Center, Code 662, Greenbelt, MD 20771, USA
[10] Center for Space Science and Technology, U. of Maryland Baltimore County, 1000 Hilltop Circle, Baltimore, MD 21250, USA
[11] Department of Physics and Astronomy, Johns Hopkins University, 3400 N. Charles Street, Baltimore, MD 21218, USA
[12] Center for Research and Exploration in Space Science and Technology, NASA/GSFC, Greenbelt, MD 20771, USA
[13] IRAP, CNRS, Université de Toulouse, CNES, 9 Avenue du Colonel Roche, 31028 Toulouse, France
[14] Institut de Ciències del Cosmos (ICCUB), Universitat de Barcelona (UB), c. Martí i Franquès, 1, 08028, Barcelona, Spain
[15] Dep. de Física Quàntica i Astrofísica (FQA), Universitat de Barcelona (UB), c. Martí Franquès, 1, 08028, Barcelona, Spain
[16] Institut für Astronomie und Astrophysik, Universität Tübingen, Sand 1, D-72076 Tübingen, Germany
[17] Inter University Centre for Astronomy & Astophysics (IUCAA), Ganeshkhind, Pune 411007, India

Received XXXX; accepted XXXX

ABSTRACT

Context. Ultraluminous X-ray sources (ULXs) are luminous non-nuclear X-ray point sources embedded in galaxies. Their luminosities exceeding $10^{39}\,\mathrm{erg\,s^{-1}}$ potentially require sub-Eddington accretion by objects with masses from $\sim10^2\,M_\odot$ to $\sim10^4\,M_\odot$ or supercritical accretion beyond the Eddington limit by stellar mass black holes or neutron stars. As such, ULXs are excellent laboratories for extreme accretion flows in X-ray binaries and, in some cases, potential candidates for intermediate-mass black holes. The first catalog by the eROSITA instrument on board the *Spectrum-Roentgen-Gamma* mission provides the most complete X-ray view of the whole of the western Galactic hemisphere and is therefore an excellent resource in which to find new ULXs.

Aims. We identified ULXs by searching for X-ray counterparts in the $\sim10^5$ local galaxies of the *HECATE* catalog in the footprint of the first eROSITA all-sky survey. The catalog is unaffected by X-ray selection biases. We characterized the completeness of the sample and its contamination by unidentified active galactic nuclei (AGN) and determined the influence of source confusion. The catalog provides the basis for ULX population studies and follow-up observations that can be used to perform a more detailed investigation of individual sources and variability.

Methods. We searched for X-ray point sources exceeding the ULX threshold in *HECATE* galaxies while excluding the nuclear regions of the galaxies to avoid the selection of AGN. We removed known contaminants such as supernovae, stars, and AGN, and we manually vetted all candidates to further remove potential contaminants. We derived the X-ray selection function and fraction of unidentified AGN interlopers using a simulation with subsequent source detection. By comparing our sample to other ULX catalogs, we identified previously unknown candidates and those not detected although expected from their flux, indicating source intrinsic variability.

Results. We present two samples of ULX candidates. The main sample consists of 90 sources with highly confident X-ray detections, 53 of which are identified for the first time. This sample is complete to a distance of ~7 Mpc, contains at most 29% of unknown background AGN, and is mostly unaffected by source confusion. Several candidates are newly identified even though their locations have been observed by other instruments before, and some previously reported candidates we expected to identify are absent from our sample, demonstrating the transient behavior of ULXs. Based on our list of less confident detections, we also provide an extended catalog of 260 sources identified as potential candidates for further ULX identifications. Of these, 245 are identified as potential candidates for the first time.

1. Introduction

Ultraluminous X-ray sources (ULXs) are defined as non-nuclear sources in nearby galaxies with luminosities of $\geq10^{39}\,\mathrm{erg\,s^{-1}}$, that is, larger than the Eddington luminosity of a $\sim10\,M_\odot$ black hole (BH) or neutron star (NS; see, e.g., Kaaret et al. 2017; King et al. 2023, for reviews). While sources later described as ULXs were already discovered by the first imaging X-ray telescope, *Einstein* (e.g., Fabbiano & Trinchieri 1987),

Article published by EDP Sciences, to be cited as https://doi.org/10.1051/0004-6361/202659942

it is only in recent years that we have conclusively demonstrated that some of these objects most likely constitute the extreme end of the "normal" X-ray binary (XRB) population, given their similar hardness-ratio distributions (Earnshaw et al. 2019; M. C. i. Bernadich et al. 2022; Tranin et al. 2024). This is mainly due to the detection of pulsations from several ULXs, indicating that they must harbor NS accretors that far exceed the Eddington limit (pulsating ULXs, or PULXs, e.g., Bachetti et al. 2014; Israel et al. 2017b). Most ULXs for which sufficient X-ray data are available show a common range of X-ray spectral shapes and variability properties that are unexpected from the "classic" sub-Eddington accretors in our own Galaxy (e.g., Gladstone et al. 2009; Sutton et al. 2013; Middleton et al. 2015), characteristics that are suggestive of super-critical accretion (e.g., Beloborodov 1998; Watarai et al. 2001; Poutanen et al. 2007). This super-critical accretion scenario is also supported by the presence of wind signatures in X-ray spectra (Middleton et al. 2014; Pinto et al. 2016; Kosec et al. 2021). The similarities in spectral shape and variability between PULXs and other well-studied ULXs indicate that NSs could underlie a sizable part, if not the majority, of ULXs. (e.g., Pintore et al. 2017; Walton et al. 2018; Gúrpide et al. 2021). The entire population may be heterogeneous, however, with indications for intermediate-mass black holes (IMBH; $M_{\rm BH} \sim 10^2$–$10^4\,M_\odot$) in a few very luminous objects (e.g., Webb et al. 2012; Mezcua et al. 2015).

Catalogs have played a key role in improving our understanding of the ULX population. The first ULX catalogs were by-products of the search for X-rays from low-luminosity active galactic nuclei (AGN) with *ROSAT* (Colbert & Mushotzky 1999; Roberts & Warwick 2000) and included a few tens of sources. These were then followed by systematic searches for ULXs in the *ROSAT* High Resolution Imager archives that revealed around a hundred candidates (Colbert & Ptak 2002; Liu & Bregman 2005). The number of ULX candidates has grown rapidly since then, with catalogs based on several iterations of the *XMM-Newton* serendipitous source catalog (Walton et al. 2011; Earnshaw et al. 2019; M. C. i. Bernadich et al. 2022) or derived from the *Chandra* data archives (Swartz et al. 2004; Liu 2011; Kovlakas et al. 2020) revealing hundreds of candidates. Currently, we now know of ~2000 ULX candidates, on the basis of meta-catalogs that merge the detections of ULXs in the serendipitous source catalogs of *XMM-Newton*, *Chandra*, and *Swift* (Walton et al. 2022; Tranin et al. 2024).

The ULX catalogs have provided insights into the population demographics of ULXs. Early work revealed ULXs in both elliptical and spiral galaxies, with an apparent correlation between the number of ULXs and the star formation rate (SFR) of individual spiral galaxies (Swartz et al. 2004; Liu & Bregman 2005). As the number of sources grew, the incidence of ULXs per unit mass was found to be higher for lower-mass spiral galaxies (Walton et al. 2011). The number of ULXs in a star-forming galaxy is known to scale with the SFR and stellar mass (M_*; (Kovlakas et al. 2020)), which is consistent with population synthesis models that take into account stellar ages and metallicity. Roughly one in three galaxies host at least one ULX (see also Earnshaw et al. 2019). Catalogs have also provided target lists for further study, which is particularly important for samples of rare and interesting objects. For example, there has been a study following up on sub-samples of the most luminous and/or brightest ULXs in the search for IMBH candidates (Sutton et al. 2012), which included the first investigation of the most luminous PULX, NGC 5907 ULX (Roberts et al. 2023). The catalogs have also been used for variability studies in the search for PULX candidates (Earnshaw et al. 2018) or to constrain the possible NS fraction of the ULX population (Khan et al. 2022).

All existing ULX catalogs have strong biases originating from the serendipitous source samples they are based on. These samples are mostly based on pointed observations that do not have ULX searches as their primary goal. While many catalogs contain "complete" sub-samples that, for instance, include all candidates from galaxies for which all ULXs can be detected (excluding some regions around the nucleus), the galaxies in which they reside are not selected as representative in any way. The observations that underlie these searches are often biased toward systems that are interesting for other reasons, such as an active nucleus, galaxy interaction, or other sources of high SFR or mass. Therefore, ULX population studies can benefit immensely from a new sample of candidates based on completely unbiased X-ray observations of galaxies.

The catalog of the first eROSITA X-ray all sky survey (eRASS1) is the deepest and most uniform X-ray survey of the western Galactic hemisphere, and it enables searches for ULXs in an unbiased way. We present the first catalog of ULX-candidates from eRASS1 that is deep enough to find all active ULXs out to ~7 Mpc. In Sect. 2 we present the eRASS source catalog and our identification of ULX candidates,followed by a description of basic sample properties, such as completeness and residual contamination (Sect. 3). In Sect. 4 we discuss the limitations of the catalog and its main differences compared to other existing catalogs generated from pointed observations, and this is followed by the exploration of possible source intrinsic variability in Sect. 5. We summarize our results in Sect. 6 and provide an outlook on population studies based on our catalog in an accompanying paper (Weber et al., 2026b, hereafter paper II).

2. Identifying ULX in the eROSITA all sky survey

In this section we describe the data used for the creation of the catalog and their extraction as well as the steps undertaken to derive the parameters necessary for the identification of ULX candidates. We start with descriptions of the eROSITA survey (Sect. 2.1) and the *HECATE* catalog (Sect. 2.2), followed by a detailed explanation of the ULX candidate selection (Sect. 2.3).

2.1. The eROSITA all sky survey

eROSITA is the soft instrument on board the *Spectrum-Roentgen-Gamma* mission (Sunyaev et al. 2021). Launched on 2019 July 13 to the second Lagrange point of the Sun–Earth system, it consists of seven co-aligned Wolter type I telescope modules (TMs) combined with X-ray charge coupled devices sensitive from ~0.2 keV to ~8.0 keV, providing a field of view of ~1 degree (Predehl et al. 2021).

From 2019 December until 2022 February, *Spectrum-Roentgen-Gamma* performed an all-sky survey by rotating around its Earth-pointing axis with a period of 4 h. The passage of each location on the sky through the field of view takes ~40 s. The survey poles are roughly aligned with the ecliptic poles. Positions at the ecliptic equator are covered by six subsequent scans, while the poles are covered during each scan, resulting in exposure times from ~0.2 ks to ~4 ks respectively (Predehl et al. 2021). As eROSITA moves around the Sun, the entire sky is covered once every 6 months, or one eRASS. Access to eROSITA data is split at the Galactic longitude of Sgr A*, $l_{II} \simeq 0^\circ$. The German eROSITA consortium is responsible for the western Galactic hemisphere. Data and higher-level data products taken in this region during eRASS1 were made publicly available on 2024 January 31 (Merloni et al. 2024)[1]. Our work is based on the eRASS1 main catalog of 930203 sources detected in the 0.2–2.3 keV band, which lists general source properties such as count rates and fluxes. In this work we consider the astrometrically corrected positions, unless stated otherwise.

2.2. The HECATE galaxy sample

To identify ULXs, we needed to determine which point sources in the eRASS1 catalog are colocated with known galaxies by comparing their positions with the D_{25} regions. While Walton et al. (2022) used the *HyperLEDA* catalog (Makarov et al. 2014), Tranin et al. (2024) used the *GLADE* catalog (Dálya et al. 2018), which extends *HyperLEDA* with information from other sources. Following the approach of M. C. i. Bernadich et al. (2022), we chose the Heraklion Extragalactic Catalogue (*HECATE*) compiled by Kovlakas et al. (2021) based on the *HyperLEDA* catalog as the main source of information on galaxies in the eRASS1 footprint. *HECATE* contains the positions and distances of 204733 galaxies, with additional information on their intrinsic properties, including morphological types, luminosities, star formation rates, and metallicities. It also supplies the apparent geometric shape of the galaxies in the form of D_{25} regions, which are ellipses corresponding to the 25 mag arcsec^{-2} B band isophote, parametrized with semi-major and semi-minor axes, r_1 and r_2, and the position angle of r_1. We based our work on a revised version of *HECATE* that includes improved values for the host properties, most notably for our purposes their distances (Kyritsis et al. 2026). Since *HECATE* is based on *HyperLEDA*, which was assembled from a variety of surveys with different footprints, it is not strictly possible to reliably determine its completeness (Kovlakas et al. 2021). For B band luminosities above $\sim 10^{7.1}\,L_{\mathrm{B},\odot}$ the new version of *HECATE* is complete within 10 Mpc, and down to $\sim 10^{10.7}\,L_{\mathrm{B},\odot}$ between ∼40 Mpc and ∼50 Mpc (Kyritsis et al. 2026). Compared to *GLADE*, *HECATE* provides more robust distance estimates by accounting for deviations from the Hubble flow. This is especially important given the localized sensitivity to ULXs in the eRASS1. Additionally, *HECATE* directly provides extent information in the form of D_{25} ellipses, star formation rates, stellar masses, and metallicities, all of which can be used for further population studies (paper II).

2.3. ULX candidate identification and data reduction

To identify ULX candidates we considered all point sources in the eRASS1 catalog located within the D_{25} ellipse of *HECATE* galaxies. The positional uncertainty of the X-ray detections can be ignored for this step since it generally is small compared to the semimajor axes of the galaxies ($\lesssim 5\%$). However, we ignored all sources without positional error, that is, `RA_LOWERR`, `RA_UPERR`, `DEC_LOWERR`, or `DEC_UPERR` is `NaN`. This is necessary because the absence of these uncertainties indicates a failed point spread function fit at the source position, often caused by strong, extended emission not associated with a point source, such as present in Messier 87. We also ignored sources where detection problems are indicated by at least one of the quality flags `FLAG_SP_SNR`, `FLAG_SP_BPS`, `FLAG_SP_SCL`, `FLAG_SP_LGA`, `FLAG_SP_GC_CONS`, `FLAG_NO_RADEC_ERR`, `FLAG_NO_CTS_ERR`, and `FLAG_NO_EXT_ERR` (see Merloni et al. 2024, Sect. 5.2 and Table 5 for a description of the quality flags). These quality criteria removed ∼3.5% of sources from the eRASS1 catalog.

[1] `https://erosita.mpe.mpg.de/dr1/`

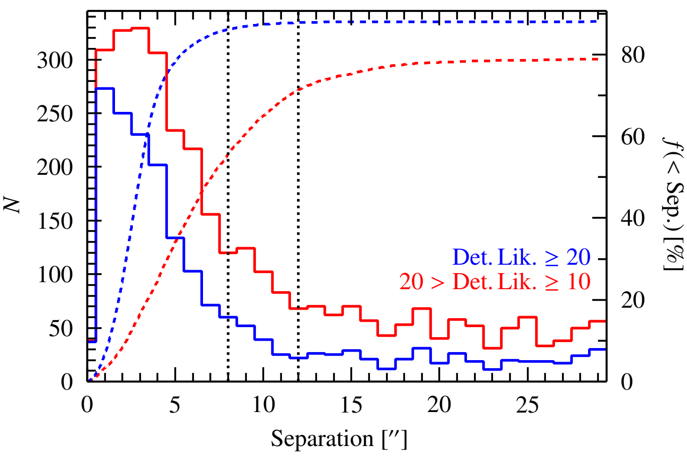

Fig. 1. Distribution of the angular separations between the cores of the *HECATE* D_{25} regions and the closest eRASS1 source (solid, left axis), and the cumulative distribution of the discrepancy between the initial and detected source position determined from a simulation of eRASS1 (dashed, right axis). We show both sets for different detection likelihood intervals. Separations of 8″ and 12″ are marked. For both sets of eRASS1 sources, the wing of central matches extends beyond 8″ to 12″. For lower detection likelihoods, a sizeable fraction of simulated sources was detected beyond 8″.

Low luminosity AGN (LLAGN) in the centers of galaxies have luminosities above the ULX threshold and can be confused with ULXs. To remove such interlopers, we excluded all sources identified too close to the nucleus of each galaxy. In Fig. 1 we show the distribution of the distances of the closest matches between the cores of the D_{25} ellipses and the eRASS1 sources. Most matches are concentrated around ∼3″, but a wing of matches extends to ∼12″. The most likely explanation for this distribution is a combination of the positional uncertainty of LLAGN in the center of some galaxies, together with the fact that the center of the D_{25} ellipse does not necessarily correspond to the nucleus of a given galaxy since it only optimizes the isophotes in the outer areas and does not relate to the surface brightness in the core. Late-type galaxies especially can have complex surface brightness distributions (see Fig. 2), which hinders the determination of the engulfing D_{25} ellipse and therefore the center of the galaxy. Additionally, a putative AGN does not necessarily have to coincide with the center of its host, which is particularly relevant for dwarf galaxies (Reines et al. 2020; Bellovary et al. 2021) and mergers (Barrows et al. 2016). In Fig. 1 we also show the positional deviation between the assumed and detected positions of simulated eRASS1 sources (see Sect. 3.1 for details regarding the simulation) and find that for detection likelihoods between 10 and 20 a significant portion of sources are detected further than 8″ from their simulated position but mostly within 12″. We thus ignored all sources closer than 12″ to the core of their respective D_{25} ellipse. After this step, 10474 sources remain in 866 galaxies.

To derive source luminosities, we extracted spectra with `srctool` version 1.76.2 from eSASS release 211214, patch level 4 (Brunner et al. 2022). To optimize the signal of the spectra, the extraction radii for the circular source regions need to be large enough to encompass most source events but small enough to minimize the inclusion of background events. In the standard data reduction performed for eRASS1 (Brunner et al. 2022),

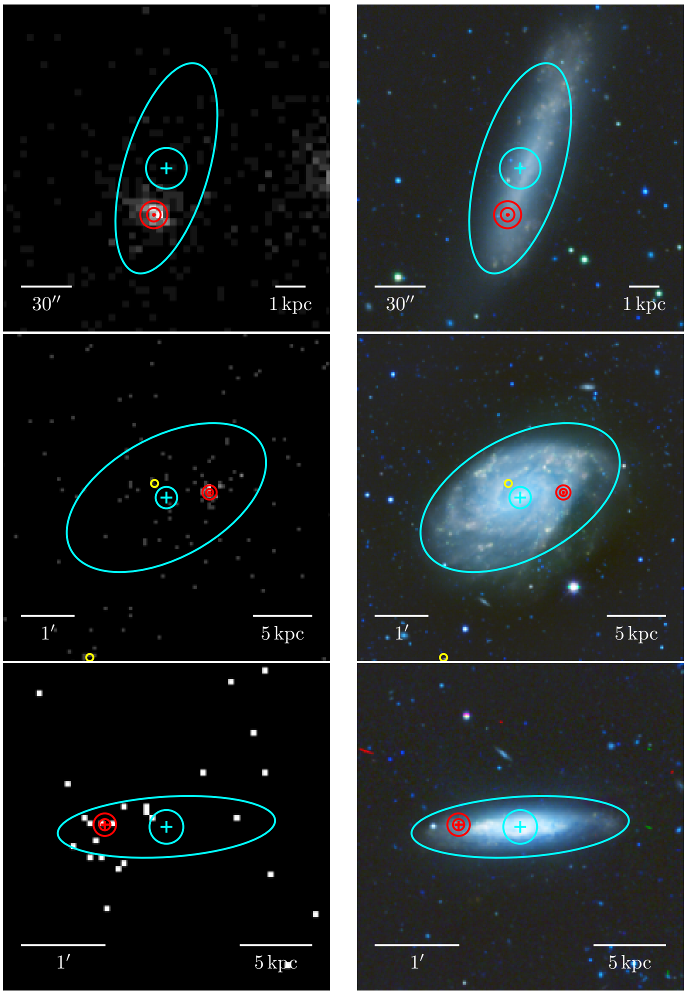

Fig. 2. X-ray and optical images of selected ULX candidates. The left column shows 0.2 keV–5.0 keV X-ray images; the right columns show optical images of the same area in the g, r, and z bands taken from DESI Legacy Imaging Survey DR8 (Dey et al. 2019). The image scale is shown in the bottom left-hand corner, the projected extent in the frame of the galaxy in the bottom right-hand corner. The cyan ellipse is the D_{25} area as listed in *HECATE*. Its central position is denoted by a cross, and the 12″ radius circular exclusion zone around the center is marked as a circle. The position of the X-ray source is marked with red circles of a 4″ and 8″ radius; other eRASS1 sources are indicated as yellow circles. The first two rows show typical examples for candidates in the main ULX sample (NGC 1824 in the first row, NGC 1255 in the second row). The third row shows a typical candidate of the extended, less secure sample in NGC 4129.

source extraction region sizes are optimized to maximize the signal-to-noise ratio with `srctool` based on a set of information from the source detection process that is not available for our analysis.[2] We therefore obtained extracted products from the first eROSITA data release[3] for all sources in the eRASS1 and found an empirical relation between the maximum likelihood count rate `ML_RATE_0` and the radii of the extraction regions, r, of

$$r = \min\left(200'', \max\left(85''.4 \cdot \mathtt{ML\_RATE\_0}^{0.28}, 23''\right)\right). \quad (1)$$

In this relation `ML_RATE_0` is a proxy for the flux, capturing the larger spread of photons across the sensor for brighter sources.

[2] The algorithm is described at `https://erosita.mpe.mpg.de/dr1/eSASS4DR1/eSASS4DR1_tasks/srctool_doc.html`
[3] `https://erosita.mpe.mpg.de/dr1/`

We extracted background spectra based on annuli centered on the source region and outside of the source circle, excluding all eRASS1 point sources from the background region, with

$$r_{\rm in} = \min\left(350'', \max\left(182''.0 \cdot \mathtt{ML\_RATE\_0}^{0.24}, 54''\right)\right) \quad (2)$$

for the inner radius and

$$r_{\rm out} = \min\left(2200'', \max\left(1063''.2 \cdot \mathtt{ML\_RATE\_0}^{0.28}, 280''\right)\right) \quad (3)$$

for the outer radius.

We derived the fluxes of all candidates by modeling their spectra. The spectra of ULXs generally have complex shapes with multiple soft components and a high energy cutoff, known to vary between observations (Kaaret et al. 2017; Fabrika et al. 2021; King et al. 2023). At this stage in the selection process the median number of detected photons per candidate was 11, which rendered a spectral fit with multiple components unfeasible. We therefore adopted a single absorbed power law with a slope of $\Gamma = 1.7$. Given their location within other galaxies, the emission of ULXs is not only affected by Galactic foreground absorption, but also absorption intrinsic to the host galaxy. Typically, the intrinsic equivalent hydrogen column of ULXs is around $\sim 10^{21}$ cm^{-2} (Kaaret et al. 2017). Given our available data, fitting a model with varying $N_{\rm H}$ proved statistically challenging. We therefore used a single absorption component with a fixed $N_{\rm H}$ of 10^{21} cm^{-2}. We fitted the 0.2 keV–5 keV spectra for all TMs except for TM5 and TM7, as for these TMs data are affected by spectral distortion caused by a light leak in the sensor chamber (Predehl et al. 2021), necessitating an increase of the lower bound to 1 keV. This energy band is narrower than the full energy range provided in the main source catalogs derived from data by *Swift* (2SXPS, Evans et al. 2020), *Chandra* (CSC2, Evans et al. 2024), or *XMM-Newton* (4XMM, Webb et al. 2020), which have been used in other recent ULX compilations. Compared to the widest available energy range of these instruments, from 0.2 keV to 12.0 keV by *XMM-Newton*, the resulting flux is reduced by ∼40%, assuming the same spectral shape. For a slope of the ULX X-ray luminosity function (XLF) of $\alpha = 1$ (Tranin et al. 2024) this reduced flux leads to an expected decrease of ULX classifications by ∼40%. The spectra of sources with a detection likelihood of 10 typically contain ∼10 net counts with a background contribution of ∼2 counts. We therefore did not extrapolate the flux to the energy bands of these other instruments as it would have inflated its uncertainty. Unless indicated otherwise, all spectral fits quoted here and in the following were performed on background subtracted spectra with ISIS, version 1.6.2-51 (Houck & Denicola 2000), and utilized Cash (1979) statistics. We derived luminosities from the best-fit fluxes using the distances of the host galaxies as listed in *HECATE*. Point sources were retained as ULX candidates if their 0.2–5.0 keV band luminosity exceeded 10^{39} erg s^{-1}, which left us with 838 ULX candidates in 784 galaxies. Choosing a more shallow (steeper) slope with $\Gamma = 1.5$ ($\Gamma = 2.0$) would have increased (decreased) the flux by ∼10%, which would have resulted in 843 (830) candidates at this stage.

2.4. Sample cleaning

The eRASS1 catalog provides information about the confidence of individual detections in the form of the detection likelihood, which was derived by fitting a calibrated point spread function profile to the measured photon distribution at the position of a putative source (Merloni et al. 2024). Generally, this likelihood scales with the number of counts available for the detection of a

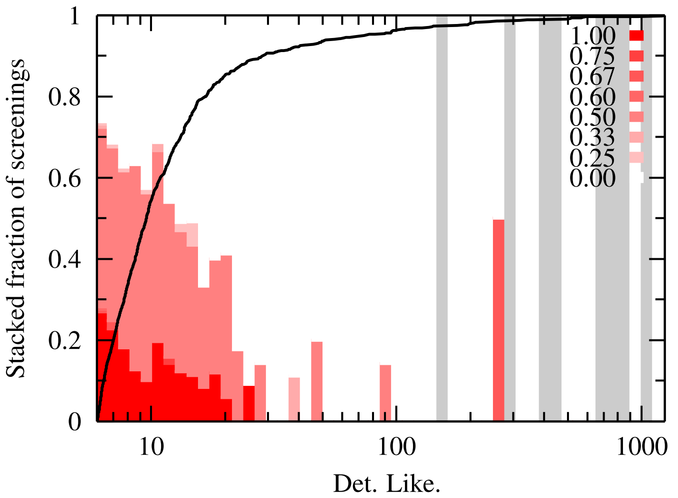

Fig. 3. Stacked bar diagram showing how often a candidate was flagged as a spurious detection compared to how often it was screened with respect to the detection likelihood. The opaqueness of the red bars (including the white areas) denote the relative number of times a source within each area was flagged as spurious. Sources were investigated between two and five times, leading to the fractions in the legend. The sizes of the bars correspond to the relative number of sources within the bin falling in the respective category. The black line in the foreground shows the cumulative distribution of the entire candidate sample. Gray areas denote empty bins. The peak at ∼250 is caused by one of two sources flagged within this bin.

source and therefore with its flux and exposure. In order to define a reliable sample of candidates, we needed to find a lower limit for this detection likelihood, above which spurious detections due to individual background photons resembling a weak point source can be ruled out. Given the complex environment in which the ULX candidates are located, such as a background of diffuse emission from the host galaxy, it is not sufficient to use purely statistical arguments at this step. To this end we conducted a manual screening process during which each of the candidates was investigated by at least two distinct and randomly assigned astronomers. Each person was provided with X-ray and optical images from eROSITA, from the Digitized Sky Survey (Lasker et al. 1996), Panoramic Survey Telescope and Rapid Response System (Chambers et al. 2016, Pan-STARRS), and the Dark Energy Survey (Dey et al. 2019, DES), similar to those in Fig. 2. Additionally, supplemental information including light curves of flux and luminosity for all four eRASS surveys (determined from the current internal version of the eRASS:4 catalog), basic source parameters, derived parameters (flux, luminosity, upper limits of flux, luminosity, and count rate), and various other information, such as potential counterparts and past observations were available. Each person could then assign a variety of flags to each candidate, indicating special properties of the source (e.g., whether the source coincides with a clear point source, is located outside of the galaxy, or is not a point source), and note comments for further discussion. See Appendix A for a complete list of available flags in the screening process. We provide the results of the screening process as columns in the published catalog, most notably `screen_flag_spurious` (see Appendix B). Figure 3 compares the detection likelihood of the candidates with the frequency of how often they were flagged as spurious detections. Based on these results, we consider sources with detection likelihoods above 20 as members of our main sample. Candidates with detection likelihoods between 10 and 20 form part of an extended sample with pending confirmation of being real X-ray detections. We ignored all other sources with detection likelihoods of less than ten. Using these limits, we identified 111 candidates in 104 galaxies in the main sample and 268 candidates in 264 galaxies in the extended sample.

Seppi et al. (2022) determined the detectability of galaxy clusters and AGN with eROSITA through a simulation with subsequent source detection. They find an overall rate of ∼1% spurious AGN detections due to random background fluctuations at a lower detection likelihood limit of 10. However, this number was derived from sources isolated from other environments, specifically not embedded in the diffuse emission of galaxies, which is the case for ULXs. The elevated rate of diffuse emission increases the number of spurious detections. Additionally, extended structure with low flux in the galaxy, such as star-forming regions, cannot be detected as such and registers as spurious point sources. Based on the manual screening, we therefore found that a more conservative minimum detection likelihood is necessary to keep our ULX samples clean from such interlopers.

To reduce the number of contaminants further, we performed an extensive search for possible counterparts of a variety of other source types, utilizing positional matching with a maximum source distance of 8″. These identifications are not mutually exclusive. Particularly, during the manual screening process, a flag could be set that duplicates the result of the automatic matching or contradicts it. Supernovae in other galaxies can exceed luminosities of 10^{39} erg s^{-1}. They occur over the entire extent of the galaxy, resulting in an appearance similar to that of ULXs. We therefore matched our candidates against the Open Supernova Catalog (Guillochon et al. 2017) and queried the NASA/IPAC Extragalactic Database (Helou et al. 1991) for known supernovae, which identified 11 counterparts. Matching against the AGN catalog of Véron-Cetty & Véron (2010), we identified three possible contaminants. To identify foreground stars we matched the samples against the Gaia DR3 catalog (Gaia Collaboration et al. 2023) to find counterparts with a parallax larger than 0, as well as the Tycho-2 Catalogue (Høg et al. 2000), and the Yale Catalog of Bright Stars (Hoffleit & Warren 1995), yielding three foreground stars in total. We also removed one of the five "fake" ULXs identified by Gutiérrez (2013) from the main sample, and one object identified as background AGN (Sutton et al. 2015). One further candidate was flagged manually during visual inspection as background AGN and seven as foreground stars. Four additional candidates were identified in galaxies with D_{25} regions that do not resemble the optical shape of the galaxy. We supply a comprehensive list of all identified contaminants in order to help future ULX searches.

After the removal of these identified contaminants, the main and extended samples consist of 90 candidates in 85 galaxies and 260 candidates in 256 galaxies respectively. Five hosting galaxies in the main sample and four hosting galaxies in the extended sample contain two candidates. Of all the candidates, 37 in our main sample and 15 in the extended sample were previously listed by Kovlakas et al. (2020), Walton et al. (2022), M. C. i. Bernadich et al. (2022), or Tranin et al. (2024). Therefore, there are 53 previously unknown ULX candidates in the main sample and 245 in the extended sample. We provide the samples and identified contaminants on the DR1 page.[4]

[4] `https://erosita.mpe.mpg.de/dr1/AllSkySurveyData_dr1/Catalogues_dr1/`

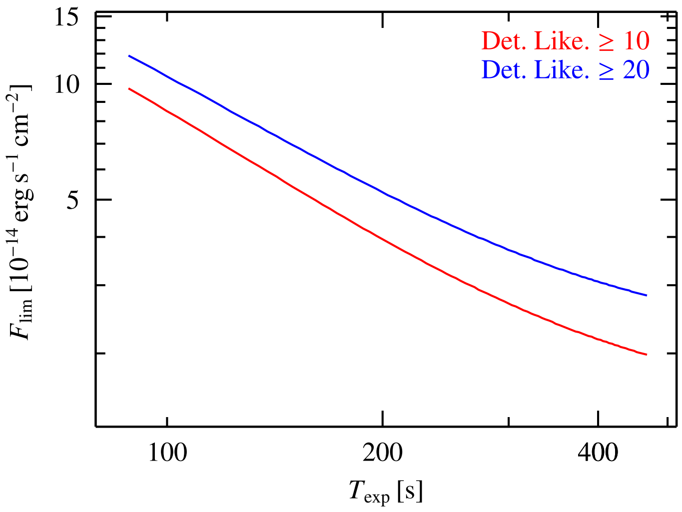

Fig. 4. Simulated limiting flux for a detection with at least 95% probability depending on the exposure time at different detection likelihood thresholds.

Table 1. Parameters for Eq. 4 to give a lower flux limit for a detection with a probability of 95% at different detection likelihoods.

Det. Like.	a	β	t_0	F_0
≥10	2.2	2.1	−55	1.4
≥20	2.2	2.0	−60	2.1

Notes. Units are: t_0: s, a: 10^{-9} erg s^{-1} cm^{-2}, F_0: 10^{-14} erg s^{-1} cm^{-2}. The fits are based on values determined from a cumulative distribution and therefore lack uncertainties.

3. The eROSITA ULX candidate sample

In this section we describe the properties of the ULX candidate sample. We start by deriving the selection function through a simulation based on which we calculate the completeness of the sample (Sect. 3.1). Using this result, we estimate in Sect. 3.2 how the sample is contaminated by background AGN.

3.1. Completeness

The effective exposure of individual eROSITA sources is a strong function of their position, both due to the survey strategy and due to strong vignetting (Sect. 2.1), implying a complex source detection behavior. To quantify this performance, we adopted the approach by Seppi et al. (2022) for our selected detection likelihood limits and the spectral shape assumed for our ULX candidates. We used the SIXTE simulation package (Dauser et al. 2019) and the eROSITA attitude for the western Galactic hemisphere to generate simulated eROSITA events of 10^5 randomly distributed sample sources. The fluxes of the sources were logarithmically uniformly distributed between 10^{-16} erg s^{-1} cm^{-2} and 10^{-11} erg s^{-1} cm^{-2} in the 0.2–2.3 keV band with an absorbed power law spectrum ($\Gamma = 1.7$, $N_{\rm H} = 10^{21}$ cm^{-2}). This flux range ensures the coverage of the full eROSITA sensitivity range. We then processed these simulated event data with eSASS, following the same steps that were used for the creation of the eRASS1 catalog (Merloni et al. 2024). By comparing the detected simulated sources with the input catalog, we determined the detection probability as a function of flux and exposure, and the number of false positives, that is, the sources detected by eSASS at locations on the sky where no sample source is located. Specifically, we considered a source to be detected if it is within 8″ of an input source. Using the detection likelihood thresholds 10 and 20, we could then determine the minimum flux above which at least 95% of the input sources were detected as a function of exposure time, $T_{\rm exp}$ (Fig. 4). We find that this limiting 0.2–2.3 keV flux can be described by

$$F_{\rm lim}(T_{\rm exp}) = a \cdot (T_{\rm exp} - t_0)^{-\beta} + F_0, \quad (4)$$

where t_0 and F_0 account for an offset in exposure time and flux respectively. Our best-fit parameters are given in Table 1. Since all *HECATE* galaxies have $T_{\rm exp} \geq 75$ s, all potential candidates with fluxes $\gtrsim 10^{-13}$ erg s^{-1} cm^{-2} should have been detected. For the galaxies located in areas of the sky with longer $T_{\rm exp}$, the limiting flux is $\sim 10^{-14}$ erg s^{-1} cm^{-2}.

Using Eq. (4), we converted the flux limit for each *HECATE* galaxy into a point source luminosity limit. In Fig. 5 we illustrate the maximum distance at which a ULX is detectable as a function of its position on the sky. Our result implies that for hyperluminous X-ray sources (HLX), with $L_{\rm X} \geq 10^{41}$ erg s^{-1}, our main candidate sample is complete out to ~70 Mpc, while the ULX sample is complete within ~7 Mpc. In order to estimate the luminosity dependent volume in which eRASS1 is complete, we subdivided the sky into $N_{\rm pix}$ pixels of equal area using the Hierarchical Equal Area isoLatitude Pixelization (HEALPix; Górski et al. 2005) package. For each pixel we then used Eq. 4 to determine the minimum flux necessary for a detection, $F_{\rm lim}$, and estimated the total sensitive volume down to a threshold luminosity, $L_{\rm lim}$,

$$V_{\rm tot}(L_{\rm lim}) = \sum_{i=1}^{N_{\rm pix}} \frac{1}{N_{\rm pix}} \frac{4}{3}\pi d_{i,\rm lim}^3 = \sum_{i=1}^{N_{\rm pix}} \frac{1}{N_{\rm pix}} \frac{4}{3}\pi \left(\frac{L_{\rm lim}}{4\pi F_{i,\rm lim}}\right)^{3/2}, \quad (5)$$

where $d_{\rm lim}$ is the maximum distance for each individual pixel. Evaluating the sum yields

$$V_{\rm tot}(L_{\rm lim}) = 2937\,{\rm Mpc}^3 \left(\frac{L_{\rm lim}}{10^{39}\,{\rm erg\,s^{-1}}}\right)^{3/2} . \quad (6)$$

Table 2 lists the total volumes and the number of galaxies to which eRASS1 is sensitive for various luminosity thresholds.

Table 2. Sensitive volume for different lower luminosity thresholds.

log $L_{\rm lim}$ [erg s^{-1}]	$V_{\rm tot}$ [Mpc^3]	$N_{\rm gal}$	$f_{\rm gal}$
39	3×10^3	1750	1.7%
40	93×10^3	8033	7.8%
41	3×10^6	39979	38.8%
42	93×10^6	103069	100%

Notes. The limits were calculated using Eq. 6 with $N_{\rm pix}$ = 199608. We also list the total and relative number of galaxies in *HECATE* above each luminosity threshold. Down to 10^{42} erg s^{-1} eRASS1 is sensitive to all but 26 galaxies.

3.2. Estimation of the AGN contamination

The majority of X-ray point sources detected at high Galactic latitudes are expected to be background AGN (Predehl et al. 2021). A fraction of these appear within the D_{25} regions of galaxies, but are actually located behind them. If the AGN are bright enough, they may be misidentified as ULX. Since a fraction of these AGN are not flagged by our screening (Sect. 2.3), they remain in the sample as interlopers and skew further analyses. In this section we estimate this AGN contamination.

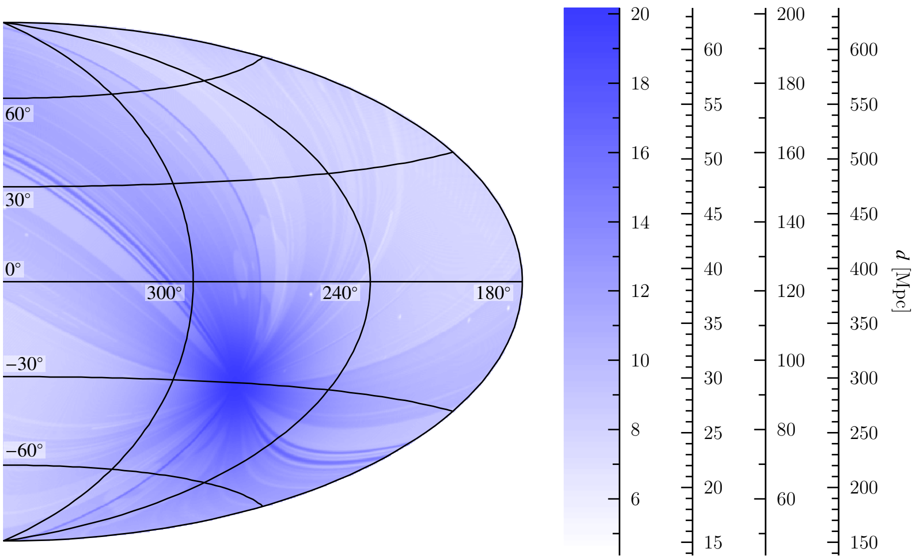

Fig. 5. Spatially resolved map of maximum distances up to which a putative ULX with a given minimum luminosity would be detected in the eRASS1 with a detection likelihood of at least 20. The four different legends apply to minimum luminosities of 10^{39} erg s^{-1}, 10^{40} erg s^{-1}, 10^{41} erg s^{-1}, and 10^{42} erg s^{-1}, from left to right. See Table 2 for numerical values of the volumes. Note that most *HECATE* galaxies are located within 200 Mpc.

Salvato et al. (2025) utilize a machine learning approach to identify optical and infrared counterparts of eRASS1 sources based on training samples not representative for ULX candidates, as they are X-ray point sources embedded in the optical disks of galaxies, rendering their photometric redshift estimates unreliable. Sources in the D_{25} regions therefore need to be investigated individually.

The sensitive flux range of eROSITA is fully covered by the well-established AGN $\log N$-$\log S$ (Gilli et al. 2007)[5]. Based on this $\log N$-$\log S$ distribution, we determined the number of AGN that would (erroneously) be identified as ULX in a given galaxy's D_{25} region. We integrated the 0.5–2.0 keV AGN XLF over the flux range corresponding to the luminosity range of ULX in each galaxy, properly taking into account each galaxy's sensitivity limit (Eq. 4). We converted the fluxes from the eROSITA band to the 0.5–2.0 keV band used by Gilli et al. (2007), by assuming the spectral shape of the AGN is an absorbed power law with $\Gamma = 1.7$ and $N_H = 10^{21}$ cm^{-2}. We determined the number of AGN expected in each galaxy, considering its area and accounting for the nuclear exclusion region, arriving at the total number of expected contaminants by summing over all galaxies. Taking into account the number of background AGN identified in the sample by catalog matching and removing them from the ULX catalogs, our results imply 26 remaining AGN interlopers in the main sample, 38 in the extended sample, and therefore 64 in the combined main and extended sample (Table 3).

Our estimate of the contaminants solely relies on the geometry of the galaxies and ignores the attenuation of background AGN by matter in the galaxy. Using typical AGN spectra (power laws with $\Gamma = 1.5$ to $\Gamma = 2.3$), absorption in the intervening galaxy can reduce the 0.2–8.0 keV flux by ∼66%, assuming a typical galaxy intrinsic $N_H = 10^{21}$ cm^{-2} (e.g., Kaaret et al. 2017). Our estimate of AGN background contaminants can therefore be considered a conservative upper limit.

We identified 41% of the sources of our main sample in other published catalogs (Kovlakas et al. 2020; Walton et al. 2022; M. C. i. Bernadich et al. 2022; Tranin et al. 2024), while in the extended sample this fraction is only 6%. This illustrates the higher fraction of contaminants in the extended sample, given its lower detection likelihood limit. By comparing the number of expected background AGN in both samples (Table 3) we make a similar observation. With the availability of eRASS:5 data and dedicated follow-up observations the validity of some of the sources in the extended sample will be confirmed in the future.

[5] Retrieved from `http://www.bo.astro.it/~gilli/counts.html` with $F_{\min} = 10^{-15}$ erg s^{-1}, $F_{\max} = 10^{-10}$ erg s^{-1}, $N_{H,\min} = 10^{20}$ cm^{-2}, $N_{H,\max} = 10^{26}$ cm^{-2}, $z_{\min} = 0$, $z_{\max} = 10$, $L_{\min} = 10^{35}$ erg s^{-1}, $L_{\max} = 10^{50}$ erg s^{-1}, no high-z decline

Table 3. Estimated contamination by AGN in the main and combined samples.

Sample	$N_{\rm ULX}$	$N_{\rm AGN}$	f
both	350	64	18%
main	90	26	29%

Notes. We determined the contamination by folding the flux-dependent probability for a detection with the XLF of Gilli et al. (2007) and integrating over all galaxies. Because we identified three specific background sources in the samples, we removed this number from the values in this table.

3.3. Source confusion

With increasing distance, the limited angular resolution of eROSITA causes clustered sources and extended regions of emission, such as star-forming regions, to be detected as single, spuriously luminous point sources. This confusion with point sources can add interlopers to the identified ULX population and skew population analyses. Compared to other samples assembled by *XMM-Newton*, *Chandra*, or *Swift*, which tend to have a better spatial resolution, this effect is more relevant at smaller distances for our sample.

Star-forming regions are typically at most ∼0.5 kpc in size (Anastasopoulou et al. 2016; Kovlakas et al. 2020). In the full eRASS1 catalog we found the smallest extended sources to be detected with an extent of ∼8″, translating to a maximum distance of ∼13 Mpc beyond which such structures cannot be distinguished from point sources. This particularly includes the XRB population, rendering them apparent ULXs with artificially inflated luminosities. Of our main sample, only 30 sources reside closer than 13 Mpc, rendering more detailed population studies focusing on this subsample statistically challenging.

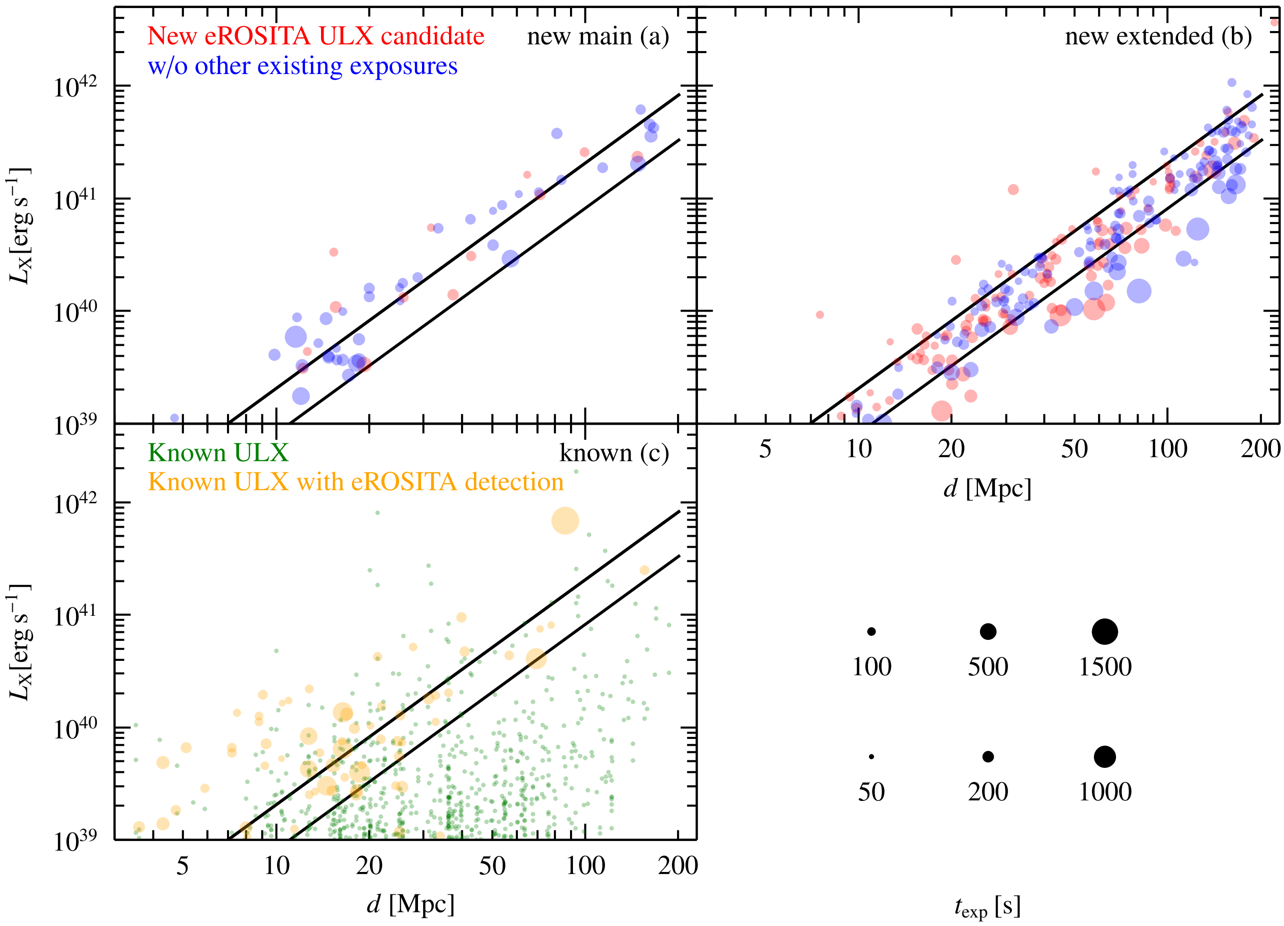

Fig. 6. Luminosity distribution with respect to distance of the main new (a), extended new (b), and known (c) sample. We representatively show the sample by Walton et al. (2022) as known sources without eROSITA detection and selected the highest available luminosity for each source from their catalog. The luminosities of known sources with eROSITA detection were determined using data from eRASS1. We converted these luminosities to the same energy band as used for eROSITA. The solid black lines denote the detection limits for the exposure at the ecliptic and the median exposure. The detection limit at the ecliptic pole is not covered by the diagram. Sources within the central exclusion zone of their hosts are not shown in the third panel. We have omitted uncertainties in the diagrams, as they would visually interfere with sizes of the circles indicating the exposure time. The average luminosity uncertainty in the first panel is ~58%, in the second panel it is ~77%, and of all eROSITA measurements in the third panel it is ~63%.

Due to the anticorrelation between the angular extent and distance of galaxies, combined with the increasing luminosity required for the detection of a point source, galaxies with smaller extent sample only the upper end of the ULX XLF. As a result, in galaxies affected more by source confusion, only the most luminous ULXs and assemblies of confused sources can be detected. To investigate the degree of extended emission regions confused as single sources in our sample we compared their luminosity with the integrated luminosity expected from the gaseous emission of their host galaxy based on standard L_X-SFR scaling relations.

We used the scaling relation of Mineo et al. (2012, their Eq. 1), $L_X/\mathrm{SFR} \simeq 8.3 \times 10^{38}\,(\mathrm{erg\,s^{-1}})/(M_\odot\,\mathrm{yr^{-1}})$, to calculate the total luminosity expected in the 0.5–2.0 keV band from the gaseous emission in all late-type ULX host galaxies. After converting the luminosities of all candidates to the same energy band, we calculated for each galaxy the ratio between the candidate luminosity and that expected from the total respective SFR.

In Fig. 7 we show the cumulative distribution of the resulting ratios. For ~85% of the galaxies, the luminosity of the ULX candidate exceeds the emission expected from the SFR by at least 1 dex, and for ~40%, it is exceeded by at least 2 dex, suggesting it is unlikely that our candidates are the result of hot gas in the hosts confused as point sources. However, the confusion of multiple luminous XRBs in the host cannot be ruled out by this method. We therefore used the recently obtained scaling relation by Kyritsis et al. (2025), $\log(L_X/\mathrm{erg\,s^{-1}}) = 0.85\log(\mathrm{SFR}/\mathrm{M_\odot\,yr^{-1}})+39.67$, which also includes the emission of resolved and unresolved XRBs, to perform the same analysis, also displayed in Fig. 7. At least ~95% of candidates exceed the luminosity expected from their hosts, and ~40% by at least 1 dex. With the area used for the extraction of the candidates only being a fraction of that of the entire galaxy, this reinforces that the candidates are likely not a result of confused emission.

Early-type galaxies harbor point sources in the form of low mass XRBs (LMXBs) but overall have a smooth distribution of their X-ray and optical emission due to their old stellar population. We avoided the selection of such galaxies by ignoring all sources flagged as extended in the eRASS1. AGN outflows or galactic superwinds may form diffuse emission clumps that can be confused with point sources. We therefore tested the hosts of all 13 candidates of our main sample identified in early-type galaxies for the presence of AGN. None of these hosts are listed in the AGN catalog of Véron-Cetty & Véron (2010),

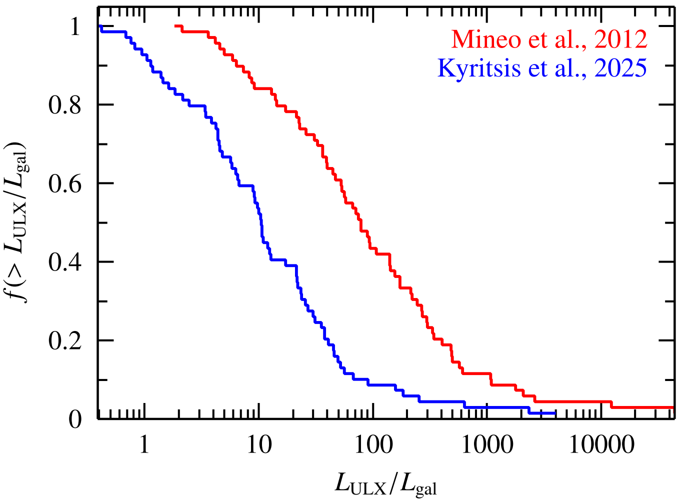

Fig. 7. Cumulative distribution of the ratio between the ULX luminosity $L_{\rm ULX}$ and the total luminosity $L_{\rm gal}$ of their respective host galaxies expected from 0.5–2 keV scaling relations for late-type galaxies (Mineo et al. 2012; Kyritsis et al. 2025).

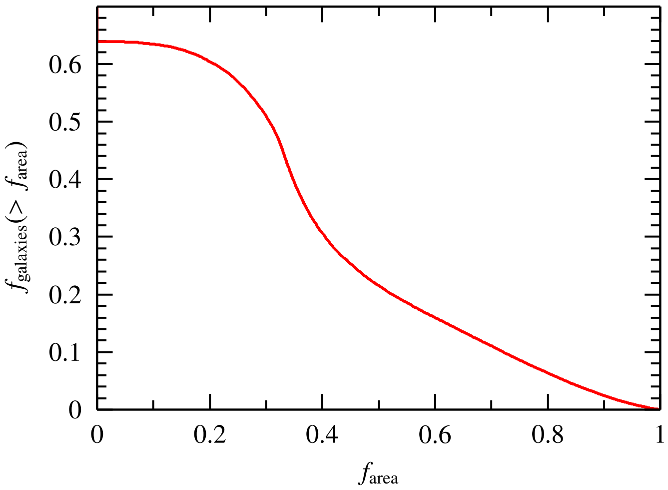

Fig. 8. Cumulative distribution of the fractional area covered by eROSITA in each galaxy. For ∼36% of the galaxies, $f_{\rm area}=0$.

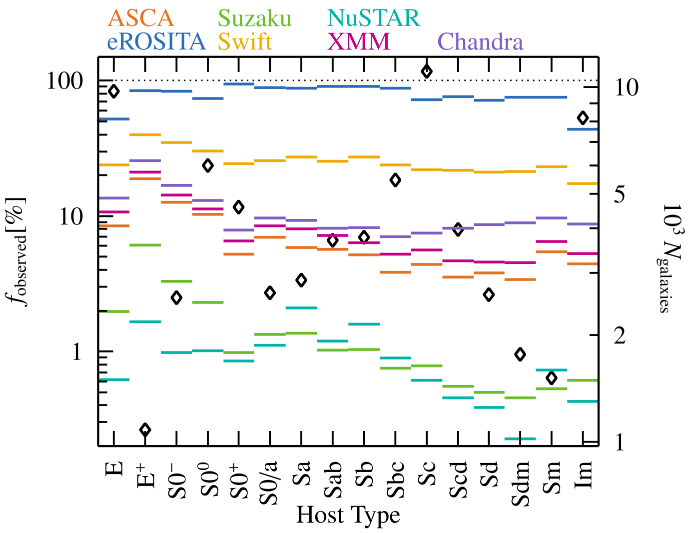

Fig. 9. Fraction of galaxies on the western Galactic hemisphere listed in *HECATE* observed by other X-ray instruments to any degree before the end of eRASS1. Galaxies without a morphological type in *HECATE* have been omitted. For eROSITA only galaxies for which r_1 exceeds the nuclear exclusion zone are considered. The diamonds show the total number of *HECATE* galaxies for each type with the axis on the right hand side.

while *HECATE* classifies NGC 1439 and NGC 4762 as AGN. Only one of the galaxies, NGC 2235, has an eRASS1 source listed at its center. The ULX in this galaxy was also identified by Walton et al. (2022). We therefore consider confusion with gaseous structures unlikely for the majority of our sample. As for the candidates in late-type galaxies, confusion of multiple point sources cannot be ruled out by this method.

4. The eROSITA ULX sample in the context of previous searches

In recent years the combined archival data of current X-ray observatories was used to identify ∼2000 ULX candidates (Kovlakas et al. 2020; M. C. i. Bernadich et al. 2022; Walton et al. 2022; Tranin et al. 2024). The necessary observations of galaxies by these instruments were generally carried out for unrelated scientific rationales. While offering substantial depth for each observation, the number of observed galaxies is limited and their selection highly biased. Utilizing data from eRASS1, we could mitigate the biased selection by trading against overall depth. In Table 4 we provide the key properties of our catalog and contrast them with these other recent samples.

The detectability of galaxies generally correlates with their optical flux and therefore decreases with distance. Since eROSITA is, down to 10^{39} erg s^{-1}, mostly sensitive to galaxies in the local Universe, the choice of the host galaxy catalog does not influence the overall result, as long as they equally cover this local range, which is the case for all catalogs listed in Table 4. We choose *HECATE* because it offers the most robust distance estimates, which directly enters the calculation of the ULX candidate luminosities, as well as robust estimates for SFR, stellar mass and metallicity, enabling further studies between the ULX population and their hosting environment (see paper II).

The completeness of X-ray selected catalogs is often expressed as the area covered down to a limiting flux. The completeness of ULX catalogs is a combination of that of the host galaxy sample and that providing the X-ray detections, and is therefore difficult to derive. Additionally, the choices for the extent of galaxies and the nuclear exclusion zone influences the completeness of ULX catalogs. The nature of ULXs provides a natural lower luminosity threshold. Therefore ULX studies typically state the farthest distance up to which all sources down to this luminosity are detected. This ignores the fact that pencil beam surveys are categorically insensitive to most galaxies.

With the eROSITA survey this aspect is drastically different. In principle eROSITA is sensitive to all *HECATE* galaxies in the footprint of eRASS1, which amounts to $\sim10^5$ objects. However, to avoid the inclusion of central AGN, an area around the core of the galaxy is typically excluded from the search. Given the coarser spatial resolution of eROSITA, we require this region to be larger compared to past studies. As a result, with increasing distance a larger fraction of galaxies is fully engulfed by this exclusion zone, decreasing the effective fractional area $f_{\rm area}$ sensitive to our ULX search. In Fig. 8 we show the cumulative distribution of $f_{\rm area}$ in each galaxy. For ∼36% of all observed galaxies $f_{\rm area}=0$, for ∼22% at least half of the area is covered.

Table 4. Comparison between the fundamental properties of the ULX catalog derived in this work and past studies.

Work[a]	This work	T24	W22	B22	K20
Base catalog(s)[b]	eRASS1	4XMM-DR11/CSC2/2SXPS	4XMM-DR10/CSC2/2SXPS	4XMM-DR9	CSC2
Energy range[c] [keV]	0.2–5	0.2–12/0.5–7/0.3–10	0.2–12/0.5–8.0[1] /0.3-10	0.2–12	0.5–8
Nuclear zone[d] [″]	12	>3	9/6.1/9	>3	3
Galaxy catalog[e]	*HECATE*	*GLADE*	*HyperLEDA* & CNG	*HECATE*	*HECATE*
Search area[f]	D_{25}	$D_{\mathrm{Holm}} \simeq 1.26 D_{25}$	D_{25}	D_{25}	D_{25}
Total candidates[g]	90	1901 + 191[2]	1843	779	629
Host galaxies[h]	85	1303	951	517	309
Contamination[i] [%]	$\lesssim$29	$\lesssim$2	∼20	∼2	∼20
Completeness[j] [Mpc]	∼7	n/a	n/a	29	40

Notes. [(a)] The publications are abbreviated as T24: Tranin et al. (2024); W22: Walton et al. (2022); B22: M. C. i. Bernadich et al. (2022); K20: Kovlakas et al. (2020) [(b)] X-ray source catalog(s) the candidate selection was performed on [(c)] Energy range in which the stated fluxes were determined [(d)] extent of the nuclear exclusion region, variable size for T24 and B22 [(e)] Galaxy catalog(s) used for the host identification [(f)] Parameter used for the optical extent of the galaxies [(g)] Total number of ULX candidates [(h)] Number of galaxies hosting the candidates [(i)] Fraction of unknown contaminants [(j)] Distance limit up to which the catalog is complete in X-rays, ignoring the completeness of galaxies [(1)] Energy range for the ACIS. For the HRC it is 0.2–10 keV [(2)] Tranin et al. (2024) state the number of ULXs and HLXs separately

In Fig. 9 we compare the number of galaxies in the western Galactic hemisphere observed by past and current X-ray observatories to the number of galaxies for which eROSITA has $f_{\mathrm{area}} > 0$, resolved by their morphological type. We limit ourselves to the ∼65% of galaxies for which *HECATE* provides morphological information. Overall, eROSITA provides the best coverage among all types of galaxies, apart from irregulars and ellipticals exceeding 70%, up to more than 90%. Interestingly, for elliptical galaxies the fraction is smaller than for other types of galaxies. This indicates that ellipticals generally have a smaller apparent extent, which is likely related to the selection function of *HECATE* favoring such galaxies at farther distances. In contrast, the instruments utilized for recent ULX catalogs, *Swift*, *XMM-Newton*, and *Chandra*, on average cover only ∼30%, ∼10%, and ∼10% of the galaxies, respectively, without accounting for the central exclusion zone utilized by these other studies.

The main advantage for basing a ULX search on the eRASS1 is this unbiased selection of galaxies. Nearby galaxies have larger extents and therefore larger f_{area}. Additionally, the survey is more sensitive at these closer distances. Therefore, the majority of all galaxies within this local volume up to ∼7 Mpc is covered by our ULX search. In contrast, searches based on pencil-beam surveys, resulting in deeper exposures and more ULX candidates, generally provide farther completeness limits for their observed galaxies, but the set of targeted galaxies is substantially lower and more affected by selection biases.

The definition of the area of a galaxy directly influences the number of candidates and AGN interlopers picked up during the selection procedure. Generally, the density of ULXs follows the density of the stellar population in a given galaxy (Wang et al. 2016; Kovlakas et al. 2020; Tranin et al. 2024), which is peaked in the center and drops toward the outer area. The choice of the central exclusion zone therefore disproportionally influences the total number of ULXs a search can recover. In contrast, the spatial density of AGN interlopers is constant. Therefore, larger nuclear zones increase the fraction of AGN contaminants in the ULX sample, leading to the observed anticorrelation between the nuclear zone and number of candidates in Table 4 and the more severe contamination in our sample in particular.

Similarly, larger extents of galaxies naturally accumulate more AGN interlopers in the ULX sample. To illustrate this effect, we calculated the number of interlopers per galaxy depending on their extent, relative to the D_{25} regions. As shown in Fig. 10, choosing the Holmberg radius instead of the D_{25} isophote increases the contamination by ∼59%. We therefore conclude that the drawback of the increased number of AGN interlopers would outweigh the gain in additional candidates.

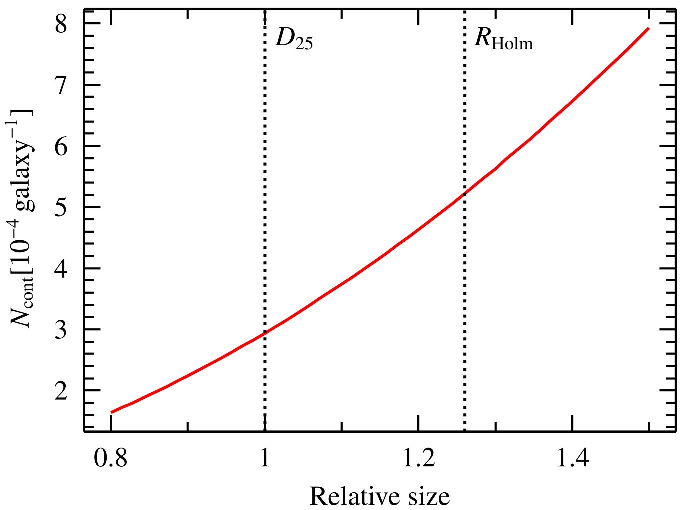

Fig. 10. Average number of expected background AGN contaminants per galaxy in the eROSITA sample as a function of the relative size of the ellipses defining the galaxy area. The D_{25} ellipses are used as the reference, with their extent and that of the Holmberg radius also marked in the figure. We expect an increase of ∼59% in size when choosing the Holmberg radius instead of D_{25}.

5. Evidence of variability in ULXs

Dedicated observatories do not only provide much longer observation durations compared to eROSITA, but especially *Swift* repeatedly captures data of multiple targets over a longer time span. This observing pattern enables variability studies (e.g., Walton et al. 2022; M. C. i. Bernadich et al. 2022; Brightman et al. 2023; Tranin et al. 2024). In fact, the variable nature of ULXs can often cause them not to appear as such. Walton et al. (2022) identified several sources that show peak luminosities above the ULX threshold but are also been found to be less luminous in other observations.

Table 5. Number of candidates in the main sample previously identified by other studies.

Work[a]	detection expected[b]	detected (unique)[c]	expected & detected[d]
T24	206	46 (23)	43 (22)
W22	285	31 (29)	29 (28)
B22	57	17 (15)	11 (11)
K20	76	18 (16)	15 (15)

Notes. [(a)] Publications are abbreviated as T24: Tranin et al. (2024); W22: Walton et al. (2022); B22: M. C. i. Bernadich et al. (2022); K20: Kovlakas et al. (2020) [(b)] Number of sources that are expected to be detected, by converting the fluxes to the eROSITA energy band, compared to the lower flux limit determined based on Sect. 3.1, and considering the D_{25} regions and the nuclear exclusion zone [(c)] Number of sources in each work for which a counterpart in our main sample was identified within a radius of 8″. eROSITA's inferior spatial resolution can lead to the identification of multiple candidates, and therefore the number of unique eROSITA matches is given in parenthesis [(d)] Number of sources that were expected to be detected and were identified

To test for such changes in luminosity we converted the fluxes from past studies to the eROSITA band and compared them to the sensitivity estimates given in Sect. 3.1. We thus derived subsamples that we expected to be also present in our sample. For the sample by Walton et al. (2022) we selected the peak fluxes and used the energy band of the respective instrument. We list the resulting identifications in Table 5, which indicates that we only identified a small fraction of the expected sources.

Thirteen of the 90 candidates in the main sample have not been previously identified as ULX but were observed before the end of eRASS1 by at least one of *ASCA* (25′), *Chandra* (15′), *NuSTAR* (6′), *Suzaku* (9′), *Swift* (12′), or *XMM-Newton* (15′), with assumed fields of view in parentheses, possibly indicating strong luminosity variation, given the better sensitivity of these missions. In Fig. 6 we mark such sources as well as previously known candidates that we expected to identify, given their flux reported in the literature. Most of the known undetected candidates tend to be far below the median sensitivity line, and hence they would not have registered in eRASS1 if they maintained their luminosity. Undetected ULXs with reported fluxes near our sensitivity limit must have faded into the background. This behavior shows that ULXs, in general, can be characterized as highly variable on the timescale of months or years. Even though the physics of supercritical accretion disks is still poorly understood, this timescale aligns with observations of LMXBs driven by disk instabilities (Dubus et al. 2001; Lasota 2001; Heinke et al. 2025), and type II outbursts of HMXBs fueled by changes in the circumstellar disk of the donating Be star (Reig 2011; Neumann et al. 2023). The XLF of LMXBs shows a break below the ULX threshold (Sarazin et al. 2000; Kim & Fabbiano 2004; Humphrey & Buote 2008; Kim & Fabbiano 2010; Wang et al. 2016), suggesting that HMXBs could be the dominant contribution of binary systems to the ULX population. This suggestion aligns with the observed variability and the detection of pulsations from ULXs (Bachetti et al. 2014; Israel et al. 2017b), while some of the more persistent sources could still be powered by an IMBH. Strong variability was also found in other known ULXs (Motch et al. 2014; Walton et al. 2015; Brightman et al. 2016; Earnshaw et al. 2020, 2022), potentially as a result of the propeller effect (Tsygankov et al. 2016; Earnshaw et al. 2020; Middleton et al. 2023), tying into the picture of a sizeable portion of the ULX population being powered by NSs. Alternative explanations proposed for the long superorbital periods observed in some ULXs involve the precession of the NS itself (Vasilopoulos et al. 2020) or of structures within the accretion flow, such as a warped disk (Motch et al. 2014) or outflowing material (Middleton et al. 2018, 2019; Khan et al. 2022).

eROSITA performed multiple observations of each source, limited to ~40 s, separated by 4 h intervals and repeated between 6 and roughly 1000 times at the survey equator and pole respectively. In our main sample the candidate with the shortest $T_{\rm exp}$ was observed for only ∼130 s, while the most observed one has $T_{\rm exp}$~3300 s. For our main sample, the median number of total detected counts is 20, which does not permit any further variability study. In future studies data from all five available eROSITA surveys (eRASS1 through eRASS5) can be used to constrain the variability of the candidates on a half-year cadence.

6. Summary and outlook

We used the main eRASS1 catalog (Sect. 2.1) to identify ULXs in the D_{25} ellipses of *HECATE* galaxies (Sect. 2.2). By ignoring all sources closer than 12″ to the core of the D_{25} regions, we avoided the selection of AGN. Using extracted spectra, we calculated the flux of each candidate in Sect. 2.3, and using the distance of the putative host galaxy, we calculated the luminosity. To identify other known contaminants, we matched our list of candidates to external databases and catalogs, which let us remove supernovae, AGN, and stars (Sect. 2.4). Inspecting all initial candidates manually led us to two samples of ULX candidates. With 90 candidates, the main sample consists of sources with a detection likelihood above 20, and this sample can be used in further population studies. We also identified 260 candidates with detection likelihoods between 10 and 20, which are likely contaminated by significant amounts of spurious detections.

To characterize the sensitivity of our selection scheme, we performed a simulation of eRASS1 based on actual eROSITA attitude data, followed by source detection identical to that used for the main eRASS1 catalog (Sect. 3.1). The resulting flux limit indicates that our ULX catalog is complete up to $d \sim 7$ Mpc, while we expect all HLXs in known galaxies within 70 Mpc to be detected, if they exceed the flux limit at the time of observation. The simulation, combined with the $\log N$-$\log S$ of AGN, allowed us to constrain the number of unidentified contaminants from background AGN to at most ~29% in our main sample (Sect. 3.2). By comparing the angular extent and distances of the observed galaxies to the spatial resolution of eROSITA, we derived a distance of $d \sim 13$ Mpc for the onset of source confusion. We also considered the properties of the hosting galaxies and find this issue unlikely to be relevant for the main sample (Sect. 3.3). Interestingly, we also find that a significant number of already known ULXs are absent from our sample, even though their reported fluxes are well within the eROSITA sensitivity range. We interpret the absence of these sources as an indication of variability being a common property among ULXs. The archival data from pointed observations and the rich multi-survey data obtained by eROSITA will be useful for performing a more systematic analysis of this variability.

We have identified 53 new ULX candidates in our main sample and 245 in the extended sample in other recent ULX catalogs. With the indiscriminate selection of galaxies distributed over an entire hemisphere, our catalog is unaffected by biases regarding properties of the host galaxies, such as their morphological type. This is in contrast to previous studies that selected candidates from pointed or limited slew observations. We have also identified sources as ULXs that were observed before and not classified as such, and, vice versa, we did not identify several candidates expected from other studies, indicating variable behavior over longer timescales (Sect. 5).

While some ULXs have unambiguously been shown to be NSs in binary systems (Bachetti et al. 2014; Israel et al. 2017a), the nature of many other sources is still unclear. The high luminosity well beyond the Eddington limit of a stellar mass BH suggests the possibility that a subpopulation of ULXs might comprise accreting IMBHs (Webb et al. 2012; Mezcua et al. 2015). If the ULX population can be broken down into several categories, a break in the luminosity function could reveal the separation of these populations. Such studies in particular require complete samples of ULXs and galaxies cleaned from contaminants and assembled in an unbiased manner. With our catalog based on eROSITA data, we have laid the groundwork for further systematic studies of the ULX population in the local Universe. In the accompanying paper II, we use our main sample and sensitivity and contamination estimates to investigate the luminosity function and relations to hosting galaxies while taking into account and correcting the effects of incompleteness and contamination.

In future works, harvesting data from eRASS1 through eRASS5 will increase the unbiased ULX sample detected by eROSITA. Using the survey's exposure, we estimate that a ULX sample selected from eRASS:5 should be complete within $\sim$14 Mpc. The half-year cadence of the individual surveys will also enable systematic variability studies of ULXs and thus shed light on the possible presence of orbital phases or spectral state transitions typical for XRBs.

Data availability

The main and extended catalog, as well as the list of identified contaminants, are available in the online version of the journal, the eROSITA DR1 webpage at `https://erosita.mpe.mpg.de/dr1/AllSkySurveyData_dr1/Catalogues_dr1/`, and at the CDS via anonymous ftp to `cdsarc.u-strasbg.fr` (`130.79.128.5`) or via `http://cdsweb.u-strasbg.fr/cgi-bin/qcat?J/A+A/XXX/XXX`.

Acknowledgements. We thank the anonymous referee for the helpful and insightful comments which improved the quality of this article. We acknowledge funding from Deutsches Zentrum für Luft- und Raumfahrt (DLR) grants 50 OR 2309, 50 QR 2103, and 50 QR 2503, and from Deutsche Forschungsgemeinschaft grant 414059771. S.H. was partly supported by the German Science Foundation (DFG grant numbers WI 1860/14-1 and 434448349). LD acknowledges funding from German Research Foundation (DFG), Projektnummer 549824807. TPR acknowledges support from the Science and Tech- nology Facilities Council (STFC) as part of the consolidated grant award ST/X001075/1. This work is based on data from eROSITA, the soft X-ray instrument aboard SRG, a joint Russian-German science mission supported by the Russian Space Agency (Roskosmos), in the interests of the Russian Academy of Sciences represented by its Space Research Institute (IKI), and the Deutsches Zentrum für Luft- und Raumfahrt (DLR). The SRG spacecraft was built by Lavochkin Association (NPOL) and its subcontractors, and is operated by NPOL with support from the Max Planck Institute for Extraterrestrial Physics (MPE). The development and construction of the eROSITA X-ray instrument was led by MPE, with contributions from the Dr. Karl Remeis Observatory Bamberg & ECAP (FAU Erlangen-Nürnberg), the University of Hamburg Observatory, the Leibniz Institute for Astrophysics Potsdam (AIP), and the Institute for Astronomy and Astrophysics of the University of Tübingen, with the support of DLR and the Max Planck Society. The Argelander Institute for Astronomy of the University of Bonn and the Ludwig-Maximilians-Universität Munich also participated in the science preparation for eROSITA. The eROSITA data shown here were processed using the eSASS software system developed by the German eROSITA consortium. This research has made use of ISIS functions (ISISscripts) provided by ECAP/Remeis observatory and MIT (http://www.sternwarte.uni-erlangen.de/isis/). This work has made use of data from the European Space Agency (ESA) mission Gaia (https://www.cosmos.esa.int/gaia), processed by the Gaia Data Processing and Analysis Consortium (DPAC, https://www.cosmos.esa.int/web/gaia/dpac/consortium). Funding for the DPAC has been provided by national institutions, in particular the institutions participating in the Gaia Multilateral Agreement. This research has made use of the SIMBAD database, operated at CDS, Strasbourg, France, and of the VizieR catalogue access tool, CDS, Strasbourg, France (DOI: 10.26093/cds/vizier). The original description of the VizieR service was published in 2000, A&AS 143, 23.

References

Aguado, D. S., Ahumada, R., Almeida, A., et al. 2019, ApJS, 240, 23
Anastasopoulou, K., Zezas, A., Ballo, L., & Della Ceca, R. 2016, MNRAS, 460, 3570
Bachetti, M., Harrison, F. A., Walton, D. J., et al. 2014, Nature, 514, 202
Barrows, R. S., Comerford, J. M., Greene, J. E., & Pooley, D. 2016, ApJ, 829, 37
Bellovary, J. M., Hayoune, S., Chafla, K., et al. 2021, MNRAS, 505, 5129
Beloborodov, A. M. 1998, MNRAS, 297, 739
Brightman, M., Hameury, J.-M., Lasota, J.-P., et al. 2023, ApJ, 951, 51
Brightman, M., Harrison, F. A., Barret, D., et al. 2016, ApJ, 829, 28
Brunner, H., Liu, T., Lamer, G., et al. 2022, A&A, 661, A1
Cash, W. 1979, ApJ, 228, 939
Chambers, K. C., Magnier, E. A., Metcalfe, N., et al. 2016, ArXiv e-prints [arXiv:1612.05560]
Colbert, E. J. M. & Mushotzky, R. F. 1999, ApJ, 519, 89
Colbert, E. J. M. & Ptak, A. F. 2002, ApJS, 143, 25
Dálya, G., Galgóczi, G., Dobos, L., et al. 2018, MNRAS, 479, 2374
Dauser, T., Falkner, S., Lorenz, M., et al. 2019, A&A, 630, A66
Dey, A., Schlegel, D. J., Lang, D., et al. 2019, AJ, 157, 168
Dubus, G., Hameury, J. M., & Lasota, J. P. 2001, A&A, 373, 251
Earnshaw, H. P., Brightman, M., Harrison, F. A., et al. 2022, ApJ, 934, 42
Earnshaw, H. P., Heida, M., Brightman, M., et al. 2020, ApJ, 891, 153
Earnshaw, H. P., Roberts, T. P., Middleton, M. J., Walton, D. J., & Mateos, S. 2019, MNRAS, 483, 5554
Earnshaw, H. P., Roberts, T. P., & Sathyaprakash, R. 2018, MNRAS, 476, 4272
Evans, I. N., Evans, J. D., Martínez-Galarza, J. R., et al. 2024, ApJS, 274, 22
Evans, P. A., Page, K. L., Osborne, J. P., et al. 2020, ApJS, 247, 54
Fabbiano, G. & Trinchieri, G. 1987, ApJ, 315, 46
Fabrika, S. N., Atapin, K. E., Vinokurov, A. S., & Sholukhova, O. N. 2021, Astrophysical Bulletin, 76, 6
Flesch, E. W. 2023, Open J. Astrophys., 6, 49
Gaia Collaboration, Vallenari, A., Brown, A. G. A., et al. 2023, A&A, 674, A1
Gehrels, N. 1986, ApJ, 303, 336
Gilli, R., Comastri, A., & Hasinger, G. 2007, A&A, 463, 79
Gladstone, J. C., Roberts, T. P., & Done, C. 2009, MNRAS, 397, 1836
Górski, K. M., Hivon, E., Banday, A. J., et al. 2005, ApJ, 622, 759
Guillochon, J., Parrent, J., Kelley, L. Z., & Margutti, R. 2017, ApJ, 835, 64
Gúrpide, A., Godet, O., Koliopanos, F., Webb, N., & Olive, J. F. 2021, A&A, 649, A104
Gutiérrez, C. M. 2013, A&A, 549, A81
Heinke, C. O., Zheng, J., Maccarone, T. J., et al. 2025, ApJS, 279, 57
Helou, G., Madore, B. F., Schmitz, M., et al. 1991, in Astrophysics and Space Science Library, Vol. 171, Databases & On-Line Data in Astronomy, ed. M. A. Albrecht & D. Egret (Dordrecht: Springer Netherlands), 89–106
Hoffleit, D. & Warren, Jr., W. H. 1995, VizieR Online Data Catalog: Bright Star Catalogue, 5th Revised Ed. (Hoffleit+, 1991)
Høg, E., Fabricius, C., Makarov, V. V., et al. 2000, A&A, 355, L27
Houck, J. C. & Denicola, L. A. 2000, in ASP Conf. Ser., Vol. 216, Astronomical Data Analysis Software and Systems IX, ed. N. Manset, C. Veillet, & D. Crabtree, 591
Humphrey, P. J. & Buote, D. A. 2008, ApJ, 689, 983
Israel, G. L., Belfiore, A., Stella, L., et al. 2017a, Science, 355, 817
Israel, G. L., Papitto, A., Esposito, P., et al. 2017b, MNRAS, 466, L48
Kaaret, P., Feng, H., & Roberts, T. P. 2017, ARA&A, 55, 303
Khan, N., Middleton, M. J., Wiktorowicz, G., et al. 2022, MNRAS, 509, 2493
Kim, D.-W. & Fabbiano, G. 2004, ApJ, 611, 846
Kim, D.-W. & Fabbiano, G. 2010, ApJ, 721, 1523
King, A., Lasota, J.-P., & Middleton, M. 2023, New Astron. Rev., 96, 101672
Kosec, P., Pinto, C., Reynolds, C. S., et al. 2021, MNRAS, 508, 3569
Kovlakas, K., Zezas, A., Andrews, J. J., et al. 2021, MNRAS, 506, 1896
Kovlakas, K., Zezas, A., Andrews, J. J., et al. 2020, MNRAS, 498, 4790
Kyritsis, E., Zezas, A., Haberl, F., et al. 2025, A&A, 694, A128
Kyritsis, E., Zezas, A., Kovlakas, K., et al. 2026, MNRAS, 548, stag522
Lasker, B. M., Doggett, J., McLean, B., et al. 1996, in ASP Conf. Ser., Vol. 101, Astronomical Data Analysis Software and Systems V, 88
Lasota, J.-P. 2001, New Astron. Rev., 45, 449

Liu, J. 2011, ApJS, 192, 10
Liu, J.-F. & Bregman, J. N. 2005, ApJS, 157, 59
M. C. i. Bernadich, Schwope, A. D., Kovlakas, K., Zezas, A., & Traulsen, I. 2022, A&A, 659, A188
Makarov, D., Prugniel, P., Terekhova, N., Courtois, H., & Vauglin, I. 2014, A&A, 570, A13
Merloni, A., Lamer, G., Liu, T., et al. 2024, A&A, 682, A34
Mezcua, M., Roberts, T. P., Lobanov, A. P., & Sutton, A. D. 2015, MNRAS, 448, 1893
Middleton, M., Gúrpide, A., & Walton, D. J. 2023, MNRAS, 519, 2224
Middleton, M. J., Fragile, P. C., Bachetti, M., et al. 2018, MNRAS, 475, 154
Middleton, M. J., Fragile, P. C., Ingram, A., & Roberts, T. P. 2019, MNRAS, 489, 282
Middleton, M. J., Heil, L., Pintore, F., Walton, D. J., & Roberts, T. P. 2015, MNRAS, 447, 3243
Middleton, M. J., Walton, D. J., Roberts, T. P., & Heil, L. 2014, MNRAS, 438, L51
Mineo, S., Gilfanov, M., & Sunyaev, R. 2012, MNRAS, 426, 1870
Motch, C., Pakull, M. W., Soria, R., Grisé, F., & Pietrzyński, G. 2014, Nature, 514, 198
Neumann, M., Avakyan, A., Doroshenko, V., & Santangelo, A. 2023, A&A, 677, A134
Pinto, C., Middleton, M. J., & Fabian, A. C. 2016, Nature, 533, 64
Pintore, F., Zampieri, L., Stella, L., et al. 2017, ApJ, 836, 113
Poutanen, J., Lipunova, G., Fabrika, S., Butkevich, A. G., & Abolmasov, P. 2007, MNRAS, 377, 1187
Predehl, P., Andritschke, R., Arefiev, V., et al. 2021, A&A, 647, A1
Reig, P. 2011, Ap&SS, 332, 1
Reines, A. E., Condon, J. J., Darling, J., & Greene, J. E. 2020, ApJ, 888, 36
Roberts, T. P., Walton, D. J., Mackenzie, A. D. A., Heida, M., & Scaringi, S. 2023, MNRAS, 525, 3330
Roberts, T. P. & Warwick, R. S. 2000, MNRAS, 315, 98
Salvato, M., Wolf, J., Dwelly, T., et al. 2025, A&A, 704, A344
Sarazin, C. L., Irwin, J. A., & Bregman, J. N. 2000, ApJ, 544, L101
Seppi, R., Comparat, J., Bulbul, E., et al. 2022, A&A, 665, A78
Sunyaev, R., Arefiev, V., Babyshkin, V., et al. 2021, A&A, 656, A132
Sutton, A. D., Roberts, T. P., Gladstone, J. C., & Walton, D. J. 2015, MNRAS, 450, 787
Sutton, A. D., Roberts, T. P., & Middleton, M. J. 2013, MNRAS, 435, 1758
Sutton, A. D., Roberts, T. P., Walton, D. J., Gladstone, J. C., & Scott, A. E. 2012, MNRAS, 423, 1154
Swartz, D. A., Ghosh, K. K., Tennant, A. F., & Wu, K. 2004, ApJS, 154, 519
Tranin, H., Webb, N., Godet, O., & Quintin, E. 2024, A&A, 681, A16
Tsygankov, S. S., Mushtukov, A. A., Suleimanov, V. F., & Poutanen, J. 2016, MNRAS, 457, 1101
Vasilopoulos, G., Lander, S. K., Koliopanos, F., & Bailyn, C. D. 2020, MNRAS, 491, 4949
Véron-Cetty, M. P. & Véron, P. 2010, A&A, 518, A10
Walton, D. J., Fürst, F., Heida, M., et al. 2018, ApJ, 856, 128
Walton, D. J., Gladstone, J. C., Roberts, T. P., et al. 2011, MNRAS, 414, 1011
Walton, D. J., Harrison, F. A., Bachetti, M., et al. 2015, ApJ, 799, 122
Walton, D. J., Mackenzie, A. D. A., Gully, H., et al. 2022, MNRAS, 509, 1587
Wang, S., Qiu, Y., Liu, J., & Bregman, J. N. 2016, ApJ, 829, 20
Watarai, K.-y., Mizuno, T., & Mineshige, S. 2001, ApJ, 549, L77
Webb, N., Cseh, D., Lenc, E., et al. 2012, Science, 337, 554
Webb, N. A., Coriat, M., Traulsen, I., et al. 2020, A&A, 641, A136

Appendix A: Screening flags

In the following we list the flags available during the manual screening process.

- Spurious detection: Indicates whether the detection of the X-ray source itself is spurious.
- Foreground star: Indicates that the X-ray detection was caused by either an X-ray bright foreground star in the Milky Way or optical loading.
- Optical Point source: Indicates that the X-ray detection is associated with an optical point source that could not be clearly identified as a foreground star
- Diffuse X-ray emission: Indicates that the X-ray detection is embedded into an area of increased diffuse radiation
- Wrong D_{25} region: Indicates that the D_{25} region in the *HECATE* does not fit the optical structure of the hosting galaxy
- Nuclear source: Indicates that X-ray detection is associated with the core of a galaxy
- Star-forming region: Indicates that the X-ray detection is embedded in an area of potential star-forming activity as determined from the optical images of the hosting galaxy
- Background source: Indicates that the X-ray detection is likely not associated with the hosting galaxy but rather an object in the background
- Wrong morphological type: Indicates that the morphological type listed in the *HECATE* is likely wrong
- Interacting galaxy: Indicates that the galaxy is gravitationally interacting with at least one other galaxy

Table A.1. Amount of flags assigned during the manual screening at the 50% and 100% thresholds.

Min. detection likelihood	6	10	20
Spurious detection	53; 15	38; 10	6; 0
Background source	34; 7	27; 6	16; 5
Foreground star	5; 1	7; 1	9; 2
Star-forming region	37; 11	36; 12	34; 13
Diffuse X-ray emission	44; 9	45; 11	36; 6
Interacting galaxy	5; 2	8; 3	9; 3
Wrong D_{25} region	13; 1	13; 2	15; 3
Nuclear source	6; 0	8; 0	12; 1
Wrong morphological type	2; 0	3; 0	2; 0
Optical point source	14; 5	17; 7	18; 9

Notes. The flag assignments are listed for different detection likelihood thresholds. Sources with negative eROSITA quality flags have been removed before the screening.

Appendix B: Column description

B.1. Main and extended sample

`IAUNAME`: IAU Name of the source in the eRASS1 catalog Merloni et al. (2024)

`RAJ2000, DEJ2000`: Equatorial coordinates from the eRASS1 [°]

`screen_background{,_n}`: Number of times the source was flagged as background source and how often it was investigated

`screen_diffuse{,_n}`: Number of times the source was flagged as diffuse region of emission and how often it was investigated

`screen_interacting{,_n}`: Number of times the hosting galaxy was flagged as interacting with another galaxy and how often it was investigated

`screen_nuclear{,_n}`: Number of times the source was flagged in the center nuclear region of the hosting galaxy and how often it was investigated

`screen_optical{,_n}`: Number of times the source was flagged as counterpart to an optical source and how often it was investigated

`screen_sfr{,_n}`: Number of times the source was flagged as associated with a star-forming region and how often it was investigated

`screen_flag_spurious{,_n}`: Number of times the source was flagged as spurious detection and how often it was investigated

`screen_star{,_n}`: Number of times the source was flagged as associated with a star and how often it was investigated

`screen_wd25{,_n}`: Number of times the D_{25} region of the galaxy was flagged as incorrect and how often it was investigated

`screen_wmorph{,_n}`: Number of times the morphological type of the hosting galaxy was flagged as incorrect and how often it was investigated

`host_{M,L}b`: Absolute *b*-band magnitude and luminosity of the hosting galaxy [mag, $L_\odot$] calculated from HECATE data

`erass1_{tstart,tstop}`: First/last moment the source was observed during eRASS1 [days since eroday 1, MJD 51544]

`erass1_t`: Midpoint of all eRASS1 observations [days since eroday 1, MJD 51544]

`erass1_dt`: Time difference between first and last observation during erass1 [days]

`erass1_exposure_{0,_8,_9}`: Total exposure time during eRASS1 for the spectra of all TMs combined, TMs 1–4 & 6, and TMs 5 & 7

`cumulative_angle_area{,_norm}`: Cumulative sensitive area for one quadrant of all HECATE galaxies combined and integrated from the center to the D_{25} limit over the angle starting from the semimajor axis to the source [arcsec^2] and normalized to the unit circle for each galaxy

`cumulative_radial_area{,_norm}`: Cumulative sensitive area of all HECATE galaxies combined and integrated radially from the center to the source [arcsec^2] and normalized to the unit circle for each galaxy

`eccentricity`: Eccentricity of the D_{25} region of the hosting galaxy

`phi`: Position angle of the source with respect to the semimajor axis of the hosting galaxy

`r_abs`: Absolute angular separation of the source to the galaxy center [°]

`r_gal`: Absolute angular separation between the core of the hosting galaxy and the D_{25} ellipse in the direction of the source [°]

`r_norm`: Angular separation between the core of the hosting galaxy and the source normalized by the separation from the core to the D_{25} ellipse

`fmin{,_ulx}`: Minimum flux [$\mathrm{erg\,s^{-1}\,cm^{-2}}$] and luminosity required for a detection of any source with a likelihood of at least 20 in the hosting galaxy and for a ULX detection

`{,e_}counts`: eROSITA X-ray counts extracted from the spectrum and associated uncertainty calculated using the mechanism by Gehrels (1986) [$\mathrm{erg\,s^{-1}}$]

`ecf_{0,8,9}`: Energy conversion factor for all TMs, TMs 1–4 &6, as well as TMs 5 & 7, 0.2 keV–5.0 keV

`{,e_,E_}flux`: 0.2 keV–5.0 keV band flux with lower and upper uncertainty [erg s^{-1} cm^{-2}]
`{,e_,E_}lum`: 0.2 keV–5.0 keV band luminosity with lower and upper uncertainty
`{,e_}rate`: 0.2 keV–5.0 keV count rate determined from extracted spectra withuncertainties calculated using the method by Gehrels (1986)
`{,e_,E_}Chandra_HR_{hm,hs,ms}`: Hardness ratios in the bands used by the CSC2 and the associated upper and lower uncertainties
`{,e_,E_}Swift_HR{1,2}`: Hardness ratios in the bands used by the 2SXPS and the associated upper and lower uncertainties
`{,e_,E_}XMM_HR{1,2,3,4}`: Hardness ratios in the bands used by the 4XMM DR13 and the associated upperand lower uncertainties
`f_milliquas`: Flag indicating a match in the Milliquas catalog version 8 Flesch (2023)
`milliquas_ids`: List of potential Milliquas counterparts as Name
`f_sdss`: Flag indicating a match in the SDSS DR15 catalog Aguado et al. (2019)
`sdss_ids`: List of potential counterparts in the SDSS DR15
`f_simbad_star`: Flag indicating a match with a star type object in the Simbad database
`simbad_star_ids`: List of potential counterparts with type star in the Simbad database
`f_walton`: Flag indicating a match in the catalog by Walton et al. (2022)
`f_bernadich`: Flag indicating a match in the catalog by M. C. i. Bernadich et al. (2022)
`bernadich_ids`: Counterpart in the catalog by M. C. i. Bernadich et al. (2022) in the SRCID column
`f_kovlakas`: Flag indicating a match in the catalog by Kovlakas et al. (2020)
`kovlakas_ids`: Counterpart in the catalog by Kovlakas et al. (2020) in the name column
`f_tranin_hlx`: Flag indicating a match in the HLX sample by Tranin et al. (2024)
`tranin_hlx_ids`: Counterpart in the HLX sample by Tranin et al. (2024) in the iauname column
`f_tranin_ulx`: Flag indicating a match in the ULX sample by Tranin et al. (2024)
`tranin_ulx_ids`: Counterpart in the ULX sample by Tranin et al. (2024) in the iauname column
`erass_*`: Column directly from the eRASS1 main catalog Merloni et al. (2024)
`hecate_{,e_}d`: Distances of the hosting galaxy [Mpc] and uncertainty (Kyritsis et al., 2026, accepted)
`hecate_{ra,dec}`: Right ascension and declination of the hosting galaxy [°] (Kyritsis et al., 2026, accepted)
`hecate_logm_star`: Base-10 logarithm of the stellar mass of the hosting galaxy [$\log_{10} M_\odot$] (Kyritsis et al., 2026, accepted)
`hecate_m_star_method`: Method used to determine the stellar mass of the hosting galaxy (Kyritsis et al., 2026, accepted)
`hecate_logsfr`: Base-10 logarithm of the star formation rate of the hosting galaxy [$\log_{10} M_\odot\,yr^{-1}$] (Kyritsis et al., 2026, accepted)
`hecate_sfr_method`: Method used to determine the star formation rate of the hosting galaxy (Kyritsis et al., 2026, accepted)
`hecate_objname`: Common name of the hosting galaxy (Kyritsis et al., 2026, accepted)
`hecate_r{1,2}`: Semi-major and semi-minor axis of the hosting galaxy [′] (Kyritsis et al., 2026, accepted)
`hecate_pa`: Position angle of the D_{25} region of the hosting galaxy (Kyritsis et al., 2026, accepted)
`hecate_pgc`: PGC number of the hosting galaxy (Kyritsis et al., 2026, accepted)
`hecate_{,e_}t`: Morphological type of the hosting galaxy and uncertainty (Kyritsis et al., 2026, accepted)

B.2. Additional columns for contaminants

`f_manual`: Source manually flagged as contaminant
`f_sn`: Flag indicating a match with a known supernova in the OSNE Guillochon et al. (2017) or an object of type supernova in the NED
`sn_ids`: List of potential supernova counterparts as prefname (NED) and name (OSNE)
`f_veron`: Flag indicating a match in the catalog by Véron-Cetty & Véron (2010)
`veron_ids`: List of potential counterparts in the catalog by Véron-Cetty & Véron (2010)
`f_gaia`: Flag indicating a match with a finite parallax larger than 0 in the Gaia DR3 catalog
`gaia_ids`: List of potential Gaia DR3 counterparts as `source_id`
`f_tycho`: Flag indicating a match in the Tycho-2 catalog (Høg et al. 2000)
`tycho_ids`: List of potential counterparts in the Tycho-2 catalog
`f_yale`: Flag indicating a match in the Yale Catalogue of Bright Stars Hoffleit & Warren (1995)
`yale_ids`: List of potential counterparts in the Yale Catalogue of Bright Stars